

## Supporting Information

### Achieving One-Electron Oxidation of a Mononuclear Nonheme Iron(V)-Imido Complex

Seungwoo Hong,<sup>†,‡,#</sup> Xiaoyan Lu,<sup>†,#</sup> Yong-Min Lee,<sup>†</sup> Mi Sook Seo,<sup>†</sup> Takehiro Ohta,<sup>±</sup> Takashi Ogura,<sup>±</sup> Martin Clémancey,<sup>‡</sup> Pascale Maldivi,<sup>\*,§</sup> Jean-Marc Latour,<sup>\*,‡</sup> Ritimukta Sarangi,<sup>\*,¶</sup> and Wonwoo Nam<sup>\*,†</sup>

<sup>†</sup> Department of Chemistry and Nano Science, Ewha Womans University, Seoul 03760, Korea

<sup>‡</sup> Department of Chemistry, Sookmyung Women's University, Seoul 04310, Korea

<sup>±</sup> Picobiology Institute, Graduate School of Life Science, University of Hyogo, RSC-UH LP Center, Hyogo 679-5148, Japan

<sup>‡</sup> Université Grenoble Alpes, LCBM/PMB and CEA/BIG/CBM/ and CNRS, UMR 5249, Grenoble 38054, France

<sup>§</sup> Université Grenoble Alpes, CEA, CNRS, INAC, SYMMES, Grenoble F-38000, France

<sup>¶</sup> Stanford Synchrotron Radiation Lightsource, SLAC National Accelerator Laboratory, Menlo Park, California 94025, United States

<sup>#</sup> These authors contributed equally to this work.

E-mail: wwnam@ewha.ac.kr; ritis@slac.stanford.edu; jean-marc.latour@cea.fr; pascale.maldivi@cea.fr

## Table of Contents

<b>Experimental Section</b>	<b>S4</b>
Materials	S4
Instrumentation	S4
Generation and Characterization of Iron(V)-Imido and Iron(V)-Imido Cation Radical Intermediates	S5
Mössbauer Analysis	S5
X-ray Absorption Spectroscopy	S5
DFT Calculations	S6
Kinetic Measurements and Product Analysis	S8
Table S1	S9
Table S2	S10
Table S3	S11
Table S4	S12
Table S5	S13
Table S6	S14
Table S7	S15
Table S8	S16
Figure S1	S17
Figure S2	S18
Figure S3	S19
Figure S4	S20
Figure S5	S21
Figure S6	S22
Figure S7	S23
Figure S8	S24
Figure S9	S25
Figure S10	S26
Figure S11	S27
Figure S12	S28
Figure S13	S29

Figure S14	S30
Figure S15	S31
Figure S16	S32
Figure S17	S33
Figure S18	S34
Figure S19	S35
Figure S20	S36
Figure S21	S37
Figure S22	S38
Figure S23	S39
Figure S24	S40
References	S41

## Experimental Section

**Materials.** All chemicals, obtained from Aldrich Chemical Co. and Tokyo Chemical Industry, were the best available purity and used without further purification unless otherwise indicated. Solvents were dried according to published procedures and distilled under argon prior to use.<sup>S1</sup> Na[Fe<sup>III</sup>(TAML)] and TAML-H<sub>4</sub> (TAML = tetraamido macrocyclic ligand, 3,3,6,6,9,9-hexamethyl-2,5,7,10-tetraoxo-3,5,6,7,9,10-hexahydro-2*H*-benzo[*e*][1,4,7,10]tetraazacyclo-tridecine-1,4,8,11-tetraide) were purchased from GreenOx Catalyst, Inc. (Pittsburgh, PA, USA), and the Na[Fe<sup>III</sup>(TAML)] complex was recrystallized from an isopropanol/H<sub>2</sub>O mixture for further use.<sup>S2</sup> <sup>57</sup>Fe-enriched **1** was prepared according to the literature method.<sup>S2</sup> *N*-tosyliminophenyliodinane (PhINTs) and <sup>15</sup>N-labeled PhINTs were prepared by previously reported literature method.<sup>S3</sup>

**Instrumentation.** UV-vis spectra were recorded on a Hewlett Packard 8453 diode array spectrophotometer equipped with a UNISOKU Scientific Instruments Cryostat USP-203A for low-temperature experiments. Cold spray ionization time-of-flight mass (CSI-MS) spectra were collected on a JMS-T100CS (JEOL) mass spectrometer equipped with the CSI source. Typical measurement conditions are as follows: needle voltage: 2.2 kV, orifice 1 current: 50-500 nA, orifice 1 voltage: 0 to 20 V, ringlens voltage: 10 V, ion source temperature: 5 °C, spray temperature: -40 °C. The CSI-MS spectrum of [Fe<sup>V</sup>(NTs)(TAML<sup>+</sup>)] was observed by directly infusing the reaction solution into the ion source through pre-cooled tube under high N<sub>2</sub> gas pressure. X-band CW-EPR spectra were taken at 5 K using a X-band Bruker EMX-plus spectrometer equipped with a dual mode cavity (ER 4116DM). Low temperatures were achieved and controlled with an Oxford Instruments ESR900 liquid He quartz cryostat with an Oxford Instruments ITC503 temperature and gas flow controller. The experimental parameters for EPR spectra were as follows: Microwave frequency = 9.647 GHz, microwave power = 1.0 mW, modulation amplitude = 10 G, gain = 1 × 10<sup>4</sup>, modulation frequency = 100 kHz, time constant = 40.96 ms and conversion time = 81.00 ms. Resonance Raman spectra were obtained using a liquid nitrogen cooled CCD detector (CCD-1024x256-OPEN-1LS, HORIBA Jobin Yvon) attached to a 1-m single polychromator (MC-100DG, Ritsu Oyo Kogaku) with a 1200 grooves/mm holographic grating. Excitation wavelength of 441.6 nm was provided by He-Cd laser (Kimmon Koha, IK5651R-G and KR1801C) with 20 mW power at the sample point. All measurements were carried out in CH<sub>3</sub>CN at -40 °C. Raman shifts were calibrated with indene, and the accuracy of the peak positions of the Raman bands was ±1 cm<sup>-1</sup>. 1D <sup>1</sup>H and <sup>15</sup>N NMR and 2D <sup>1</sup>H-<sup>1</sup>H COSY spectra were measured with Bruker model digital AVANCE III 400 FT-

NMR spectrometer. All NMR spectra were recorded in CD<sub>3</sub>CN at -40 °C. Product analysis was performed using high performance liquid chromatography (HPLC, Waters 515). Quantitative analyses were made on the basis of comparison of HPLC peak integration between products and authentic samples.

**Generation and Characterization of Iron(V)-Imido and Iron(V)-Imido Cation Radical Intermediates.** The iron(V)-imido complex, [Fe<sup>V</sup>(NTs)(TAML)]<sup>-</sup> (**1**), was prepared by reacting [Fe<sup>III</sup>(TAML)]<sup>-</sup> (0.25 mM) and solid PhINTs (3 equiv) in CH<sub>3</sub>CN (2.0 mL) at 15 °C.<sup>S4</sup> The one-electron oxidants such as [Fe<sup>III</sup>(bpy)<sub>3</sub>]<sup>3+</sup> ( $E_{ox} = 1.06$  V vs SCE), tris(4-bromophenyl)ammoniumyl hexachloroantimonate, [(4-BrC<sub>6</sub>H<sub>4</sub>)<sub>3</sub>N]<sup>+</sup>SbCl<sub>6</sub> (TBPA,  $E_{ox} = 1.08$  V vs SCE), and [Ru<sup>III</sup>(bpy)<sub>3</sub>]<sup>3+</sup> ( $E_{ox} = 1.24$  V vs SCE) were added to the CH<sub>3</sub>CN solution of **1** at -40 °C, resulting that the immediate color change from dark green to deep brown due to the formation of one-electron oxidized iron(V)-imido complex, denoted as **2**, was observed. <sup>15</sup>N-labeled **1** was also prepared using PhI<sup>15</sup>NTs in CH<sub>3</sub>CN at 15 °C under the identical reaction conditions. The reaction solution was then filtered through a disk filter and kept at -40 °C for further characterization and reactivity studies.

**Mössbauer Experiments.** The Mössbauer samples consisted of frozen <sup>57</sup>Fe-enriched solutions contained in Delrin cups. Mössbauer spectra were recorded at 5 K on a low-field Mössbauer spectrometer equipped with a Janis CCR 5 K cryostat or at 4.2 K on a strong-field Mössbauer spectrometer equipped with an Oxford Instruments Spectromag 4000 cryostat containing an 8 T split-pair superconducting magnet. Both spectrometers were operated in a constant acceleration mode in transmission geometry. The isomer shifts were referenced against that of a room-temperature metallic iron foil. Analysis of the data was performed with the software WMOSS Mössbauer Spectral Analysis Software (<http://www.wmoss.org>), 2012-2013 (Web research, Edina).

**X-ray Absorption Spectroscopy.** The Fe K-edge X-ray absorption spectra of **1** and **2** were measured at the Stanford Synchrotron Radiation Lightsource (SSRL) on the unfocussed 20-pole 2 T wiggler side-station beam line 7-3 under standard ring conditions of 3 GeV and ~500 mA. A Si(220) double crystal monochromator was used for energy selection. The monochromator was detuned 55% to eliminate contributions from higher harmonics. The complexes were measured as solutions, which were transferred into 2 mm delrin XAS cells with 70 μm Kapton tape windows under synthesis conditions and were immediately frozen after preparation and stored under liquid N<sub>2</sub>. During data collection, samples were maintained

at a constant temperature of ~10 K using a Cryo Industries closed cycle cryocooler. Data were measured to  $k = 15 \text{ \AA}^{-1}$  (fluorescence mode) using a Canberra Ge 30-element array detector. Internal energy calibration was accomplished by simultaneous measurement of the absorption of a Fe-foil placed between two ionization chambers situated after the sample. The first inflection point of the foil spectrum was fixed at 7111.2 eV. The samples were monitored for photoreduction and no shift in the rising edge energy position was observed over successive scans, indicating no x-ray dose related photoreduction of the Fe center. Data presented here are 12- and 13-scan average for **1** and **2**, respectively, and were processed by fitting a second-order polynomial to the pre-edge region and subtracting this from the entire spectrum as background. A four-region spline of orders 2, 3, 3 and 3 was used to model the smoothly decaying post-edge region. The data were normalized by subtracting the cubic spline and assigning the edge jump to 1.0 at 7150 eV using the Pyspline program.<sup>S5</sup> Data were then renormalized in Kaleidagraph for comparison and quantification purposes.

Theoretical EXAFS signals  $\chi(k)$  were calculated by using FEFF version 7.<sup>S6-S8</sup> Starting structural models were obtained from DFT optimized structures for **1** and visualized in Avogadro.<sup>S9</sup> Improvement of input structure was not required since the DFT generated model provided accurate theoretical EXAFS signals. Data fitting was performed in EXAFSPAK.<sup>S10</sup> The structural parameters varied during the fitting process were the bond distance (R) and the bond variance  $\sigma^2$ , which is related to the Debye-Waller factor resulting from thermal motion, and static disorder of the absorbing and scattering atoms. The non-structural parameter  $\Delta E_0$  ( $E_0$  = the energy at which  $k$  is 0) was also allowed to vary but was restricted to a common value for every component in a given fit. Coordination numbers was systematically varied in the course of the fit but were fixed within a given fit.

**DFT Calculations.** All density functional theory (DFT) calculations have been performed with ADF 2016.<sup>S11,S12</sup> The actual electronic structure of high-valent Fe complexes may exhibit strong charge transfers with highly donating ligands, and it is the result of a subtle compromise between destabilizing electron correlation and stabilization from exchange interaction. The description of the electronic configuration is thus very delicate in DFT, which will more or less favor these two opposite terms, depending on the chosen functional. It is well known that GGAs or low-exchange hybrids will tend to favor low-spin configurations by underestimating exchange term, whereas a hybrid with a high exact exchange contribution will tend to overestimate exchange interaction.<sup>S13,S14</sup> Prior to the analysis of electronic configurations, we have thus studied three hybrid functionals with different amounts of exact exchange: B3LYP

(20 % exact exchange),<sup>S15,S16</sup> B3LYP\* (15% exact exchange)<sup>S14</sup> and a meta-hybrid TPSSH (10% exact exchange).<sup>S17,S18</sup> We have also studied BP86, a GGA functional that was successfully used for complex **1**, i.e. Fe<sup>V</sup>NTs-TAML species.<sup>S4</sup> The d<sup>2</sup> Fe<sup>VI</sup> species may give either a singlet or triplet spin state and we have explored both. Geometry optimizations were performed with these four functionals, in an unrestricted scheme, firstly in gas phase using a triple-zeta plus one polarization function basis set on Fe, and double-zeta with one polarization function on other atoms, secondly in solvent with all-electron TZ2P basis set (triple zeta +2 polarization Slater functions) for all atoms. The Grimme 3 dispersion correction was added in all cases. The solvent was modelled as a continuum (COSMO) for acetonitrile. The Normal grid accuracy was used for geometry optimizations (with Integration parameter 4). Frequencies were calculated by 2-point numerical differentiation (Integration parameter 6) on optimized geometries in gas phase, for the most stable electronic configuration of each functional. On these geometries - both solvent and gas phases - we calculated the Mössbauer parameters (isomer shift and quadrupole splitting) using an already described protocol.<sup>S19</sup> As can be seen on Table S2, both sets of optimizations (gas or solvent) give very similar structural and Mössbauer parameters, as well as spin densities. Thanks to the structural and Mössbauer experimental data available, we could conclude that the best functional able to reproduce all experimental data was B3LYP\*. The calculated Fe-N<sub>Ts</sub> frequency compared to the Raman experimental one lead to the same conclusion (Table S2). B3LYP\* gives a Fe<sup>V</sup>-TAML<sup>+•</sup> configuration as the ground state, corresponding to the broken symmetry solution of the antiferromagnetic coupling of Fe<sup>V</sup> and TAML radical. The triplet state solution was also obtained (Table S2) and we calculated a strong magnetic exchange coupling constant  $J = -797 \text{ cm}^{-1}$ , using the formula of Yamaguchi & coll.<sup>S20</sup> B3LYP favored too much local high spin density on Fe, as seen previously on the Fe<sup>V</sup>TAML system,<sup>S4</sup> yielding as the ground state a Fe<sup>IV</sup> with one radical on each ligand (TAML and NTs) while a low-lying state is a Fe<sup>VI</sup> configuration. Conversely TPSSH was able to converge only to a restricted Fe<sup>VI</sup> configuration in the singlet state, although we tried numerous initial conditions using different initial geometries or different guess conditions such as imposing initial atomic spin densities (MODIFYSTARTPOTENTIAL keyword in ADF), or using a spin flip from the triplet calculation. BP86 lead to the same conclusion as TPSSH, and this is consistent with the low (for TPSSH) or absence (for BP86) of exact exchange. Such differences between electronic configurations depending on the nature of the functional had been noticed in the description of the electronic structure of Fe<sup>V</sup> compounds.<sup>S4,S21</sup> EA and HAA for **1** and **2** were calculated from

B3LYP\*-D3 optimizations followed by numerical frequencies calculations in gas phase using a triple-zeta with one polarization function basis set on Fe, and double-zeta with one polarization function on other atoms to estimate ZPE and  $\Delta S$  terms. The electronic energy was then evaluated from these geometries by SP with B3LYP\*-D3/TZ2P in solvent (COSMO model for acetonitrile).

**Kinetic Measurements and Product Analysis.** Kinetic measurements were performed on a Hewlett Packard 8453 photodiode-array spectrophotometer at 15 °C for C–H bond amination and –40 °C for sulfimidation reactions. Reactions were run in a 1-cm UV cuvette and followed by monitoring UV-vis spectral changes of reaction solutions. Rate constants were determined under pseudo-first-order conditions (e.g., [substrate]/[**2**] > 10) by fitting the changes in absorbance at 750 nm due to **2**. Xanthene, 9,10-dihydroanthracene (DHA), indene, fluorene, and deuterated xanthene (xanthene-*d*<sub>2</sub>) were used in the C-H bond activation reactions. The natural decay of **2** was determined to be  $4.1 \times 10^{-4} \text{ s}^{-1}$  in CH<sub>3</sub>CN at 15 °C. Thioanisole and *para*-*X*-substituted (*X* = OMe, Me, Cl, and CN) thioanisole derivatives have been employed for the nitrene transfer reactions. To compare the reactivity of **2** with that of **1** in the sulfimidation reactions at the same temperature, temperature-dependent kinetic experiments were carried out. Reactions were run at least in triplicate, and the data reported represent the average of these reactions.

Products formed in the C–H bond activation reaction of fluorene by **2** were analyzed by HPLC. Fluorene (5.0 mM) was added directly to a solution of **2** (0.50 mM), and then the mixture was stirred for 30 min at 15 °C. Fluorene-NHTs was obtained as a major product with over 90% yield (based on the amount of **2** generated) under an argon atmosphere. Products formed in the nitrene transfer reaction from **2** to thioanisole were also analyzed by HPLC. Thioanisole (10 mM) was added directly to a solution of **2** (0.50 mM), and then the mixture was stirred for 10 min at –40 °C. *N-p*-tosyl-methylphenyl sulfilimine [PhS(=NTs)Me] was obtained as a major product with over 95% yield (based on the amount of **2** generated). The decay product of **2** was analyzed with UV-vis, CSI-MS, and EPR spectroscopies.



**Table S1. EXAFS Least Square Fitting Results**

complex	coordination/path	R(Å) <sup>a</sup>	σ <sup>2</sup> (Å <sup>2</sup> ) <sup>b</sup>	ΔE <sub>0</sub> (eV)	F <sup>c</sup>
<b>1</b>	1 Fe-N	1.67	492		
	4 Fe-N	1.86	311		
	8 Fe-C	2.81	438		
	16 Fe-C-N	3.08	410	2.85	0.42
	4 Fe-C	3.86	605		
	8 Fe-C-N	4.28	1211		
<b>2</b>	1 Fe-N	1.66	354		
	4 Fe-N	1.85	322		
	8 Fe-C	2.81	552	2.74	0.29
	16 Fe-C-N	3.06	498		

<sup>a</sup>The estimated standard deviations for the distances are in the order of ± 0.02 Å. <sup>b</sup>The σ<sup>2</sup> values are multiplied by 10<sup>5</sup>. <sup>c</sup>Error is given by  $\Sigma[(\chi_{\text{obsd}} - \chi_{\text{calcd}})^2 k^6] / \Sigma[(\chi_{\text{obsd}})^2 k^6]$ . The S<sub>0</sub><sup>2</sup> factor was set at 1.

**Table S2. Spin States, Resulting Energy Ordering  $\Delta E$  (kcal mol<sup>-1</sup>) of the Electronic Configurations Obtained in Singlet and Triplet States, with B3LYP, B3LYP\*, TPSSH and BP86 as well as Group Spin Densities on Fe, NTs and TAML and Fe-N Distances (Å) Compared to the Experimental Distances Given by EXAFS, Fe-N<sub>Ts</sub> Frequency (cm<sup>-1</sup>) and Mossbauer Parameters (mm s<sup>-1</sup>). Results from TZ2P/Solvent Calculations (Top of the Table) and from TZP/DZP/Gas Phase (Bottom of the Table)**

	B3LYP			B3LYP*			TPSSH		BP86		Exp. (this work)
spin	0	0	1	0	0	1	0	1	0	1	0
configuration	Fe <sup>VI</sup>	Fe <sup>IV</sup>	Fe <sup>IV</sup>	Fe <sup>VI</sup>	Fe <sup>V</sup>	Fe <sup>V</sup>	Fe <sup>VI</sup>	Fe <sup>V</sup>	Fe <sup>VI</sup>	Fe <sup>V</sup>	-
spin density											
Fe	0	1.45	1.56	0.00	0.97	0.91	0	0.67	0	0.77	-
TAML	0	-0.73	1.08	0.00	-0.69	1.03	0	1.12	0	1.12	-
NTs	0	-0.73	-0.63	0.00	-0.28	0.05	0	0.22	0	0.11	-
$\Delta E$	5.3	0	6.0	1.8	0	4.6	0	2.8	0	9.9	
distances											
Fe-N(Ts)	1.66	1.73	1.72	1.68	1.68	1.67	1.66	1.84	1.66	1.69	1.66
avg. Fe-N <sub>TAML</sub>	1.88	1.88	1.89	1.88	1.88	1.91	1.87	1.88	1.87	1.88	1.85
Mössbauer parameters											
$\Delta E_Q$	3.41	3.92	3.63	3.26	3.49	3.65	3.27	3.61	3.38	3.55	3.62
$\delta$	-0.24	-0.08	-0.15	-0.36	-0.30	-0.12	-0.32	-0.25	-0.28	-0.24	-0.34
$\nu$ (Fe-N <sub>Ts</sub> )	729			784			866		825		796
spin density											
Fe	0	1.58	1.59	0.00	0.96	0.90	0	0.67	0	0.70	-
TAML	0	-0.78	1.14	0.00	-0.67	1.05	0	1.12	0	1.02	-
NTs	0	-0.81	-0.73	0.00	-0.27	0.09	0	0.22	0	0.11	-
$\Delta E$	7.4	0	3.3	0.1	0	3.6	0	3.4	0	5.9	
distances											
Fe-N(Ts)	1.66	1.76	1.75	1.68	1.66	1.67	1.67	1.84	1.67	1.71	1.66
avg. Fe-N <sub>TAML</sub>	1.88	1.88	1.89	1.88	1.88	1.91	1.87	1.88	1.87	1.88	1.85
Mössbauer parameters											
$\Delta E_Q$	3.27	3.81	3.65	3.31	3.50	3.70	3.37	3.65	3.43	3.51	3.62
$\delta$	-0.37	-0.11	-0.21	-0.29	-0.31	-0.19	-0.41	-0.20	-0.30	-0.20	-0.34

**Table S3. Comparison of Spin Densities from Mulliken and NPA Analysis for Fe<sup>V</sup>(TAML<sup>+</sup>) as Obtained from B3LYP\* Calculation**

	Mulliken	NPA
Fe	0.97	0.88
TAML	-0.69	-0.61
NTs	-0.28	-0.28

**Table S4. Kohn-Sham Orbitals ( $\alpha$  and  $\beta$ ) Centered on the Fe Atom and HOMO-LUMO Composition from B3LYP\* Calculation: Energies (eV) and Principal Components.  $d\pi$  Represents the  $d_{xz}$ ,  $d_{yz}$  Set. In Italics: Virtual Orbitals**

$\alpha$		$\beta$	
<i>E</i> (eV)	ppal comp.	<i>E</i> (eV)	ppal comp.
-2.50	<i><math>d_{x^2-y^2}^*</math></i>	-1.95	<i><math>d_{x^2-y^2}^*</math></i>
-3.86	<i><math>d_{z^2}^*</math></i>	-3.54	<i><math>d_{z^2}^*</math></i>
-4.70	<i><math>(dyz + \pi_{NTs})^*</math></i>	-4.19	<i><math>(dyz + \pi_{NTs})^*</math></i>
-5.10	<i><math>\pi_{TAML} (LUMO)</math></i>	-4.30	<i><math>(dxz + \pi_{NTs})^*</math></i>
-6.88	<i><math>(dxz + \pi_{NTs})^*</math></i>	-6.51	$\pi_{TAML} (HOMO)$
-8.78	$d_{xy}$	-8.26	$d_{xy}$

**Table S5. C-H BDE Values of Substrates, Second-Order Rate Constants ( $k_2$ ), Apparent Second-Order Rate Constants ( $k_2'$ ) and  $\log(k_2')$  Values for the C-H Bond Activation Reaction of Various Substrates by 2 in CH<sub>3</sub>CN at 15 °C**

substrate	C-H BDE, kcal mol <sup>-1</sup>	$k_2$ , M <sup>-1</sup> s <sup>-1</sup>	$k_2',^a$ M <sup>-1</sup> s <sup>-1</sup>	$\log(k_2')$
xanthene	75.5	13	6.5	0.81
DHA	77.0	3.1	$7.8 \times 10^{-1}$	-0.10
indene	79.0	$6.4 \times 10^{-1}$	$3.2 \times 10^{-1}$	-0.49
fluorene	80.0	$2.1 \times 10^{-1}$	$1.1 \times 10^{-1}$	-0.96
xanthene- <i>d</i> <sub>2</sub>	-	1.8	-	-

<sup>a</sup>  $k_2$  was determined and adjusted for reaction stoichiometry to yield  $k_2'$  based on the number of equivalent target C-H bonds of substrates.

**Table S6. Relative Rate Constants ( $k_{\text{rel}}$ ) Determined in the Reactions of **2** with *para*-X-Substituted Thioanisoles in CH<sub>3</sub>CN at -40 °C**

X	$E_{\text{ox}},^a$ V vs SCE	$\sigma_{\text{p}}$	$k_{\text{rel}}$	$\log(k_{\text{rel}})$
OCH <sub>3</sub>	1.13	-0.27	68	1.8
CH <sub>3</sub>	1.24	-0.17	6.2	$7.9 \times 10^{-1}$
H	1.34	0	1.0	0.0
Cl	1.37	0.23	$2.6 \times 10^{-1}$	$-5.9 \times 10^{-1}$
CN	1.61	1.00	$3.7 \times 10^{-3}$	-2.6

<sup>a</sup> Taken from the reference, Park, J.; Morimoto, Y.; Lee, Y.-M.; Nam, W.; Fukuzumi, S. *J. Am. Chem. Soc.* **2012**, *134*, 3903.

**Table S7. Calculated EA and BDE (kcal.mol<sup>-1</sup>) for 1 and 2 from Electronic Energies, Zero-Point Energies and Entropies (eV). Geometry Optimizations and Frequencies from B3LYP\*-D3/DZP/TZP in Gas Phase, Followed by Single-Points with B3LYP\*-D3/TZ2P in Solvent (COSMO = Acetonitrile)**

	<b>1</b>			<b>2</b>		
	<b><sup>2</sup>1</b>	<b><sup>3</sup>1 red</b>	<b><sup>3</sup>1-H</b>	<b><sup>1</sup>2</b>	<b><sup>2</sup>2 red</b>	<b><sup>2</sup>2-H</b>
<i>E</i>	-486.617	-491.217	-491.965	-481.447	-486.617	-486.842
ZPE	14.197	14.169	14.513	14.202	14.197	14.521
TDS	2.981	2.860	2.841	2.831	2.981	2.786
		EA	BDE		EA	BDE
$\Delta H$ (kcal/mol)		106.7	85.1		119.4	86.2
$\Delta G$ (kcal/mol)		103.9	81.9		122.8	85.1

**Table S8. Spin Densities of 1, 2, Reduced 1 and 2, and 1-H and 2-H Species from B3LYP\*-D3/DZP/TZP in Gas Phase**

	<sup>2</sup> 1	<sup>3</sup> 1 red	<sup>3</sup> 1-H	<sup>1</sup> 2	<sup>2</sup> 2 red	<sup>2</sup> 2-H
Fe	0.97	1.76	1.88	0.91	0.97	1.64
NTs	-0.17	0.13	0.01	-0.25	-0.17	-0.01
TAML	0.20	0.12	0.10	-0.66	0.20	-0.64



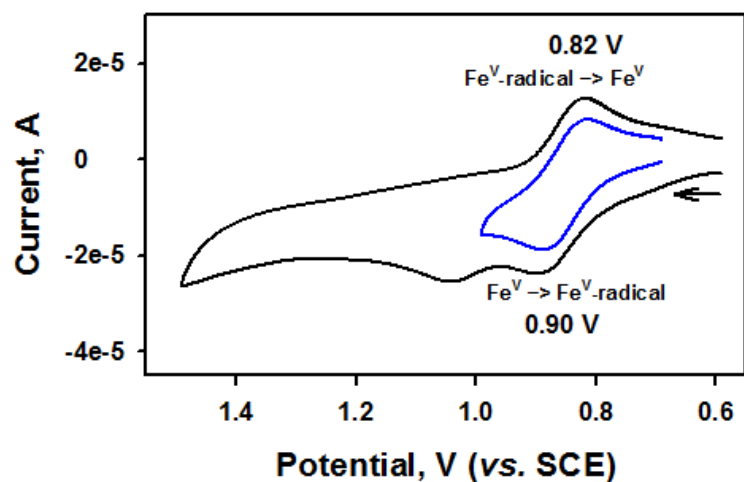


**Figure S1.** Cyclic voltammograms of  $[\text{Fe}^{\text{V}}(\text{NTs})(\text{TAML})]^-$  (**1**, 2.0 mM) in the presence of  $\text{TBAPF}_6$  (0.10 M) in  $\text{CH}_3\text{CN}$  at  $-40\text{ }^\circ\text{C}$ . A glassy carbon electrode was used as a working electrode. Scans were started to positive directions with scan rate of  $0.10\text{ V s}^{-1}$ . Oxidation potential of **1** was determined to be  $0.86\text{ V vs SCE}$ .

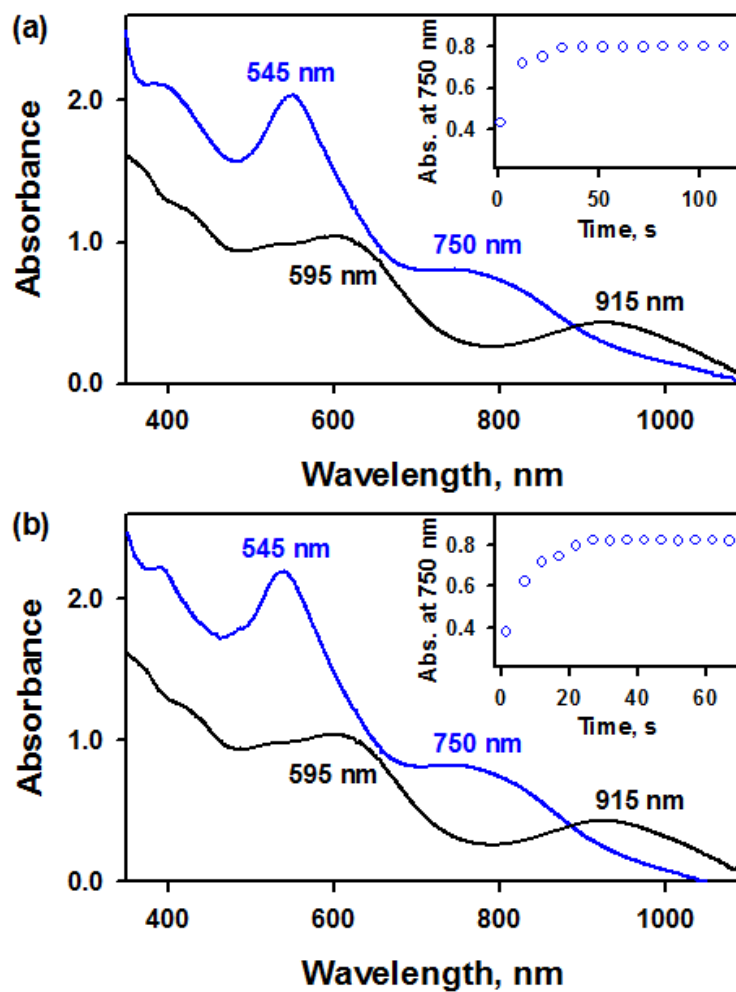


**Figure S2.** UV-vis spectra of **1** (0.20 mM, black line) and **2** (0.20 mM, blue line) in CH<sub>3</sub>CN at -40 °C. **2** was generated by adding one-electron oxidants (1.1 equiv), such as (a) (4-BrPh)<sub>3</sub>N<sup>+</sup>SbCl<sub>6</sub> (TBPA) and (b) [Fe<sup>III</sup>(bpy)<sub>3</sub>]<sup>3+</sup>, to the solution of **1** (0.20 mM) in CH<sub>3</sub>CN at -40 °C. Inset shows the time trace monitored at 750 nm due to **2**.

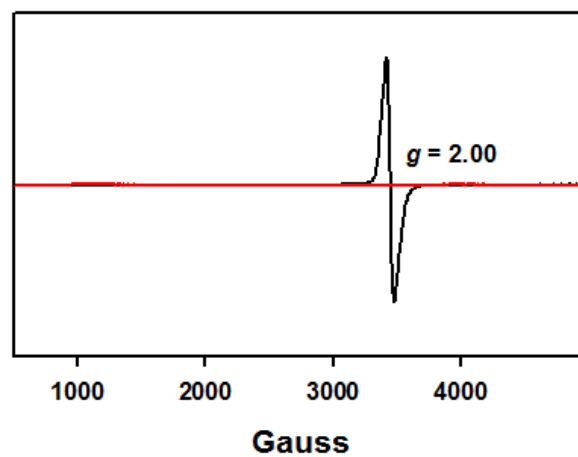


**Figure S3.** X-band CW-EPR spectra of **1** (0.50 mM, black line) and **2** (0.50 mM, red line) recorded in CH<sub>3</sub>CN at 5 K.

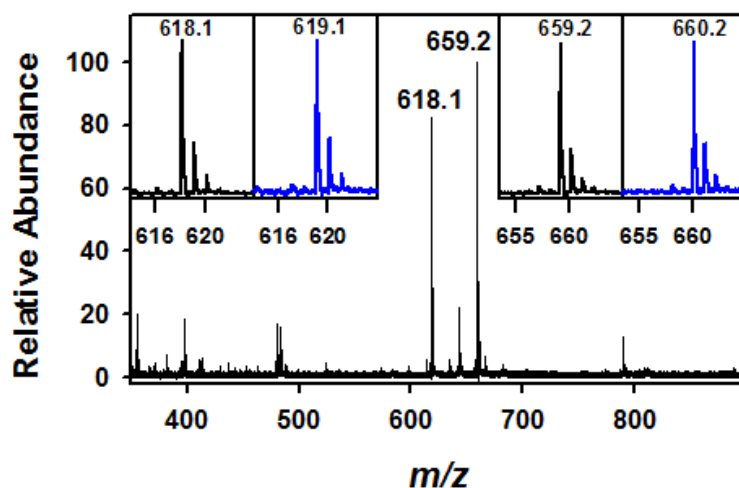


**Figure S4.** Positive mode CSI-MS spectrum of **2** obtained in the one-electron oxidation of  $[\text{Fe}^{\text{V}}(\text{NTs})(\text{TAML})]^-$  (**1**) by TBPA in  $\text{CH}_3\text{CN}$  at  $-40\text{ }^\circ\text{C}$ . The peaks at  $m/z = 618.1$  and  $659.1$  correspond to  $\{\text{Na}[\text{Fe}^{\text{V}}(\text{NTs})(\text{TAML}^+)]\}^+$  (calculated  $m/z = 618.1$ ) and  $\{\text{Na}[\text{Fe}^{\text{V}}(\text{NTs})(\text{TAML}^+)(\text{CH}_3\text{CN})]\}^+$  (calculated  $m/z = 659.1$ ), respectively. Insets show the observed isotope distribution patterns for **2**- $^{14}\text{NTs}$  (black line) and **2**- $^{15}\text{NTs}$  (blue line). **1**- $^{15}\text{NTs}$  was generated by reacting  $[\text{Fe}^{\text{III}}(\text{TAML})]^-$  with  $\text{PhI}^{15}\text{NTs}$  and then **2**- $^{15}\text{NTs}$  was generated by reacting **1**- $^{15}\text{NTs}$  with TBPA.

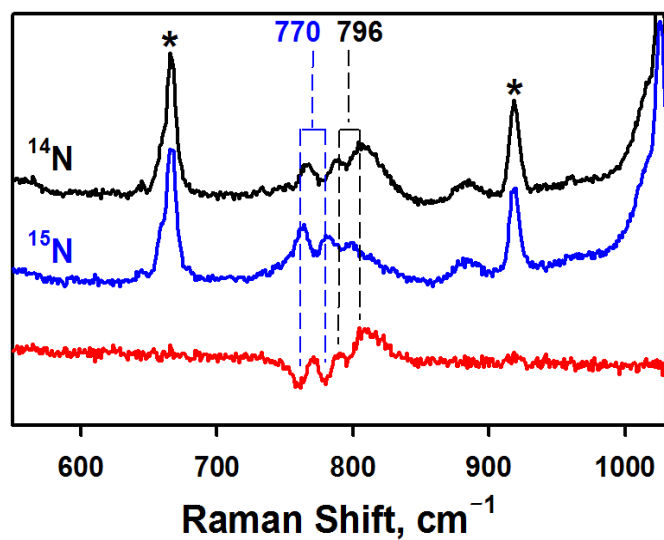


**Figure S5.** rRaman spectra of **2**-<sup>14</sup>NTs (4.0 mM, black line) and **2**-<sup>15</sup>NTs (4.0 mM, blue line) obtained upon 441.6 nm-excitation in CH<sub>3</sub>CN at -40 °C. Red line shows the spectral difference between rRaman spectra of **2**-<sup>14</sup>NTs and **2**-<sup>15</sup>NTs. The peaks marked with \* are from solvent. It should be noted that **1** also exhibited the doublet feature in rRaman spectrum (see reference 8 in Text).

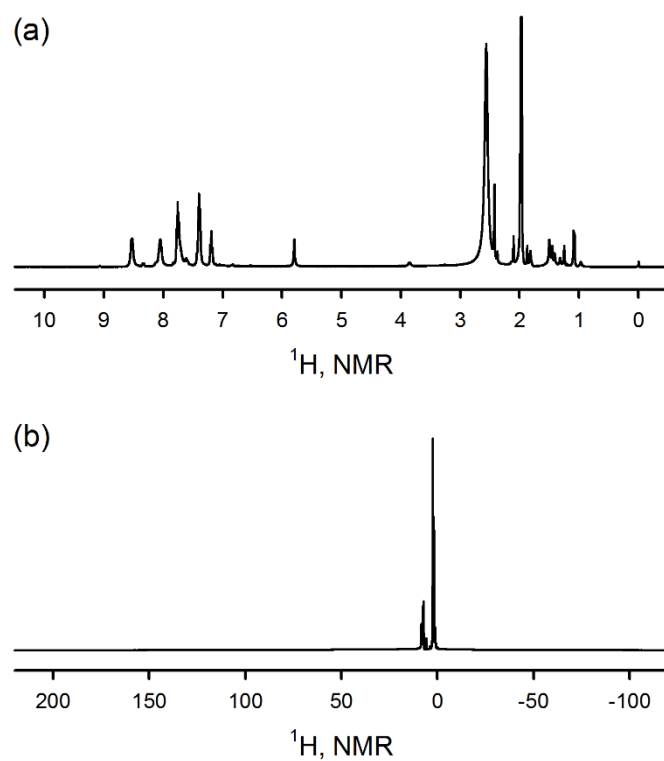


**Figure S6.**  $^1\text{H}$  NMR spectra of  $\text{Fe}^{\text{V}}(\text{NTs})(\text{TAML}^+)$  (**2**) in  $\text{CD}_3\text{CN}$  at  $-40\text{ }^\circ\text{C}$ . Spectra were recorded (a) in the diamagnetic region (from 10.5 ppm to  $-0.5$  ppm) and (b) in the paramagnetic region (from 220 ppm to  $-120$  ppm). All peaks are located in the diamagnetic region, indicating that **2** is the diamagnetic species (see Figures S7 and S8 for the assignments).

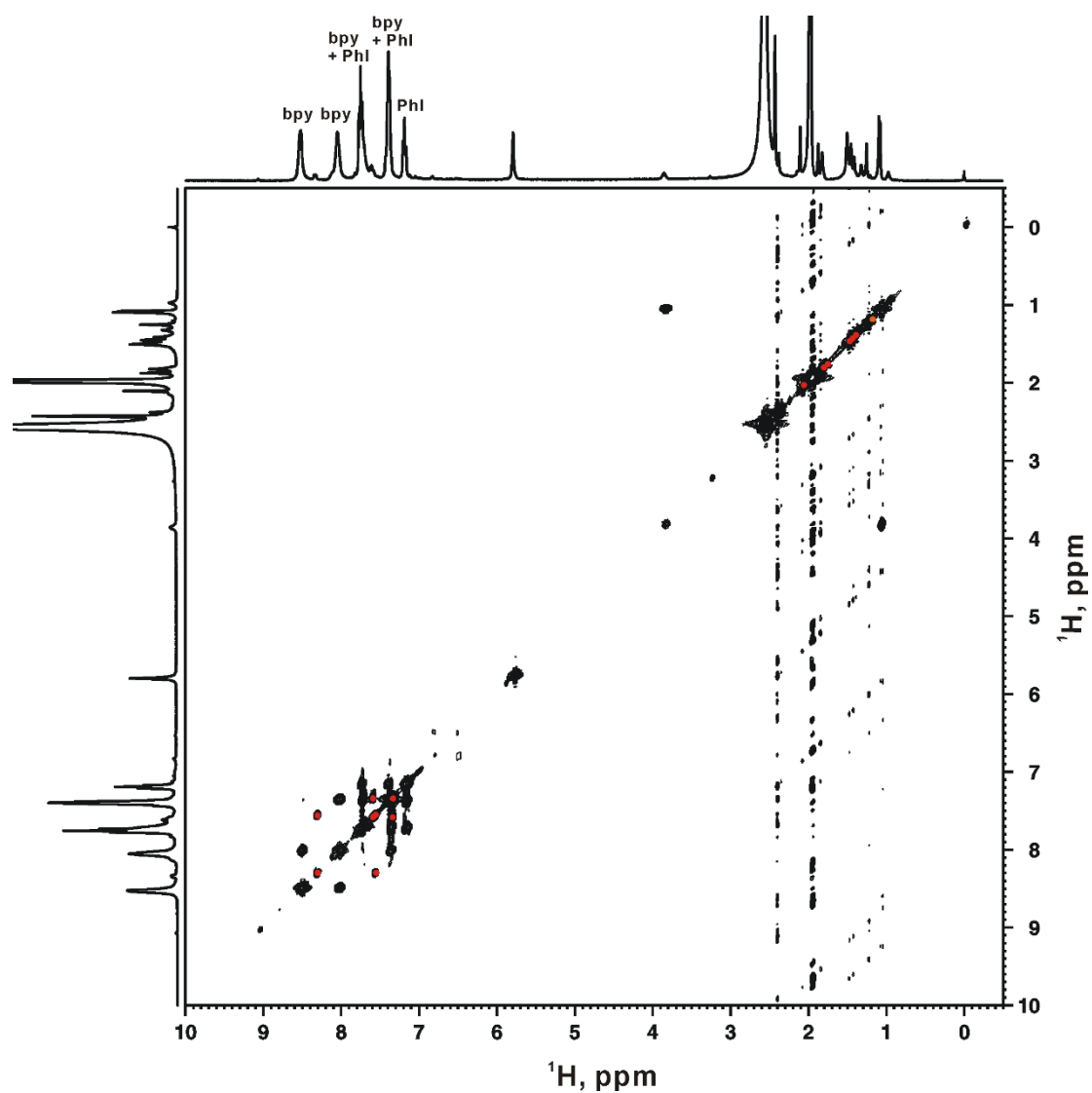


**Figure S7.** 2D  $^1\text{H}$ - $^1\text{H}$  COSY spectrum of  $\text{Fe}^{\text{V}}(\text{NTs})(\text{TAML}^{+\bullet})$  (**2**) in  $\text{CD}_3\text{CN}$  at  $-40\text{ }^\circ\text{C}$ . Peaks marked with red dots are assignable to the phenyl rings in TAML ligand and NTs, one methyl in NTs and 6 methyl group in TAML ligand (see Figure S8 for 2D  $^1\text{H}$ - $^1\text{H}$  COSY spectrum of  $[\text{Mn}^{\text{V}}(\text{O})(\text{TAML})]^-$  as a diamagnetic reference).

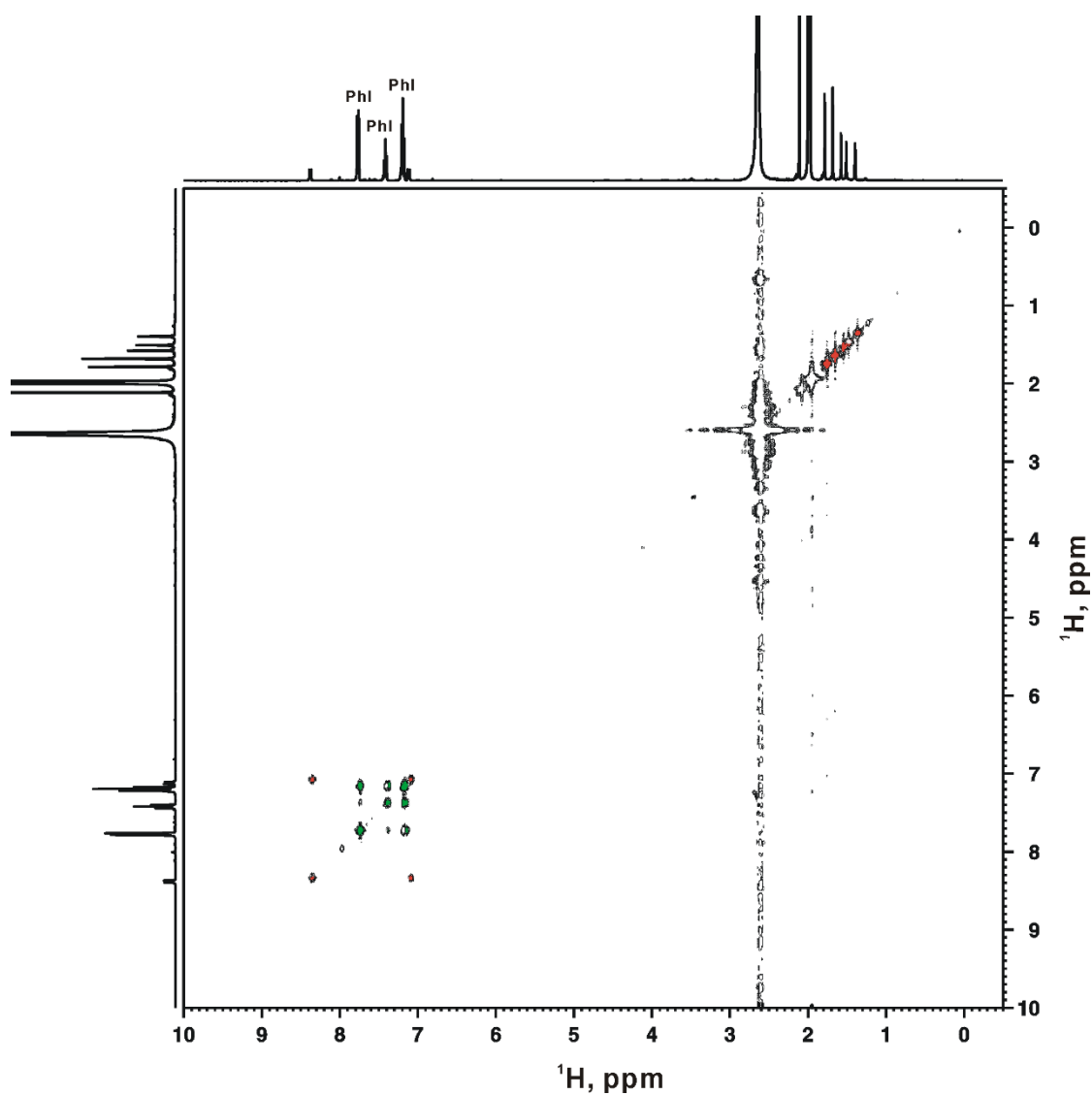


**Figure S8.** 2D  $^1\text{H}$ - $^1\text{H}$  COSY spectrum of  $[\text{Mn}^{\text{V}}(\text{O})(\text{TAML})]^-$  as a diamagnetic reference in  $\text{CD}_3\text{CN}$  at  $-40\text{ }^\circ\text{C}$ . Peaks marked with red and green colours originated from TAML ligand in  $[\text{Mn}^{\text{V}}(\text{O})(\text{TAML})]^-$  and PhI, respectively (see reference: Hong, S.; Lee, Y.-M.; Sankaralingam, M.; Vardhaman, A. K.; Park, Y. J.; Cho, K.-B.; Ogura, T.; Sarangi, R.; Fukuzumi, S.; Nam, W. *J. Am. Chem. Soc.* **2016**, *138*, 8523–8532).  $[\text{Mn}^{\text{V}}(\text{O})(\text{TAML})]^-$  was generated by reacting  $[\text{Mn}^{\text{III}}(\text{TAML})]^-$  with PhIO in  $\text{CD}_3\text{CN}$  at  $25\text{ }^\circ\text{C}$ .



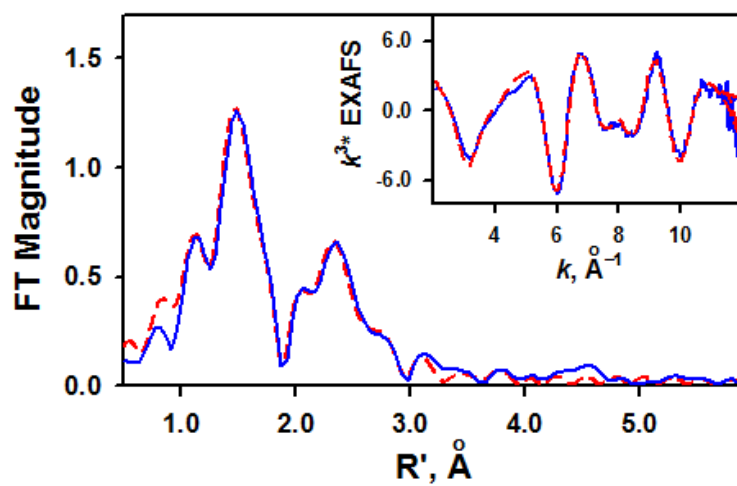
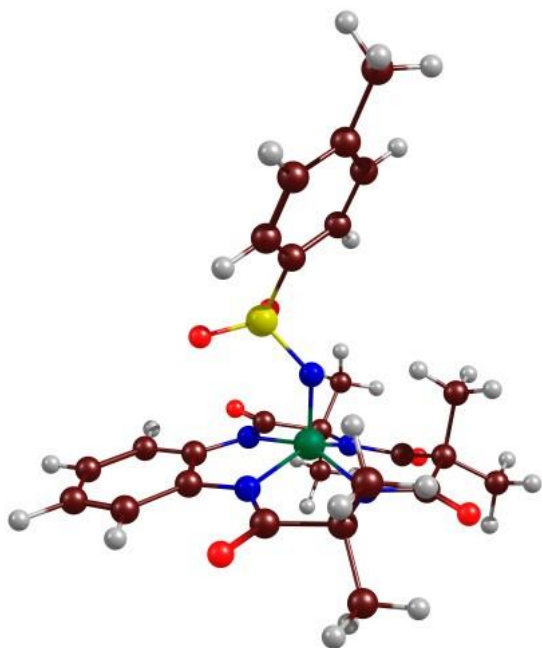


**Figure S9.** Fourier transforms of **2** (blue line) and fits (red dashed line). Inset shows EXAFS data of **2** (blue line) and fits (red dashed line).



	B3LYP*-D3	Exp.
<b>distances (Å)</b>		<b>EXAFS</b>
Fe-N(Ts)	1.68	<b>1.66</b>
avg. Fe-N <sub>TAML</sub>	1.88	<b>1.85</b>
<b>spin density</b>		
Fe	0.96	-
TAML	-0.69	-
NTs	-0.27	-
<b>Mössbauer</b>		<b>Exp.</b>
$\Delta E_Q$ (mm/s)	3.49	<b>3.62</b>
$\delta$ (mm/s)	-0.30	<b>-0.34</b>

**Figure S10.** Resulting optimized geometry from B3LYP\*-D3/ TZ2P in COSMO (acetonitrile).

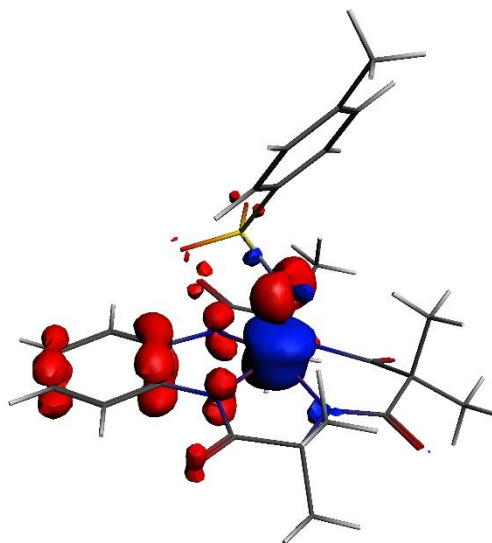


**Figure S11.** Spin density of  $[\text{Fe}^{\text{V}}(\text{NTs})(\text{TAML}^{\bullet+})]$  calculated from B3LYP\*.

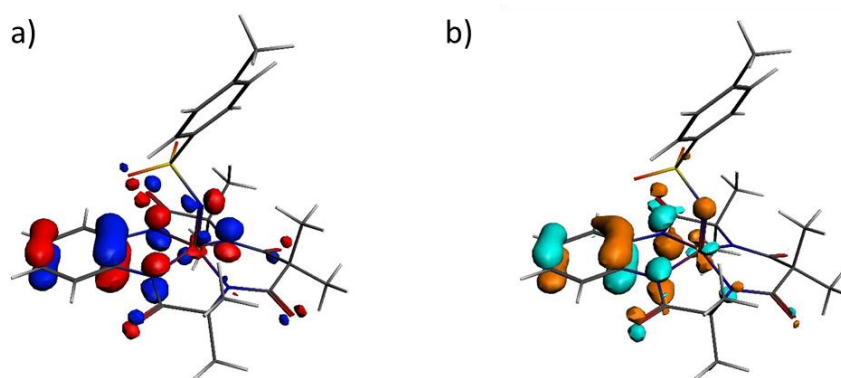


**Figure S12.** (a) HOMO and (b) LUMO of  $[\text{Fe}^{\text{V}}(\text{NTs})(\text{TAML}^{\bullet+})]$  complex from B3LYP\* calculation.

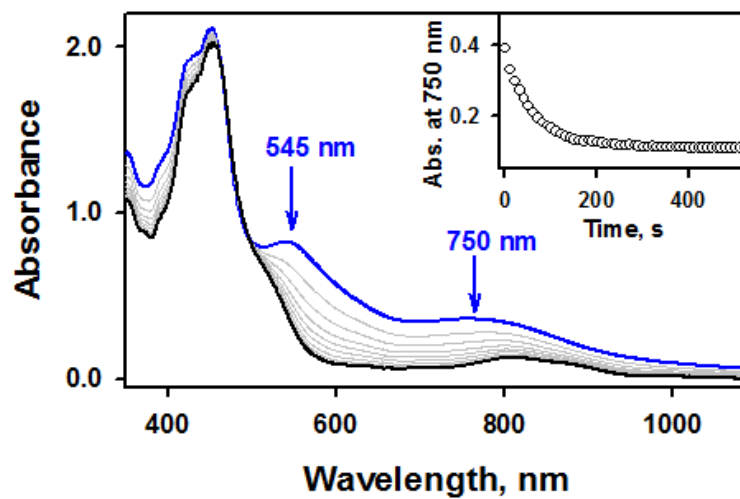


**Figure S13.** UV-vis spectral changes observed in the reaction of **2** (0.10 mM) and xanthene (1.0 mM) in CH<sub>3</sub>CN at 15 °C. Inset shows the time trace recorded at 750 nm due to **2**.

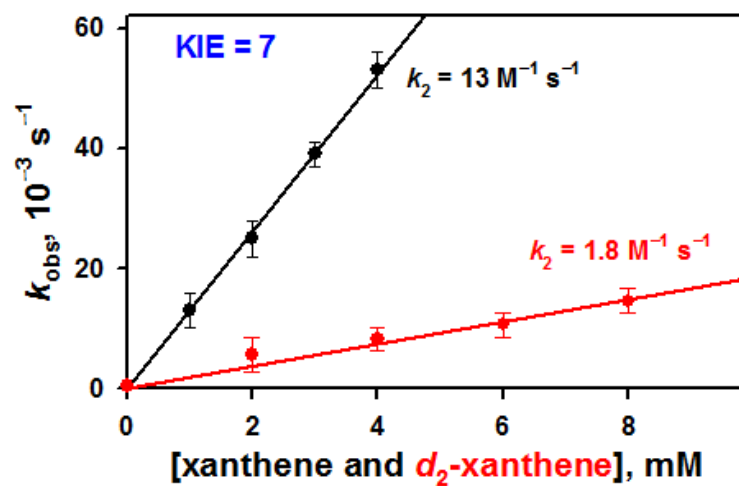


**Figure S14.** Plots of  $k_{\text{obs}}$  against concentration of xanthene (black circles), and xanthene- $d_2$  (red circles) in order to determine  $k_2$  in the oxidation of xanthene and xanthene- $d_2$  by **2** in  $\text{CH}_3\text{CN}$  at  $15^\circ\text{C}$  (also see Table S5).

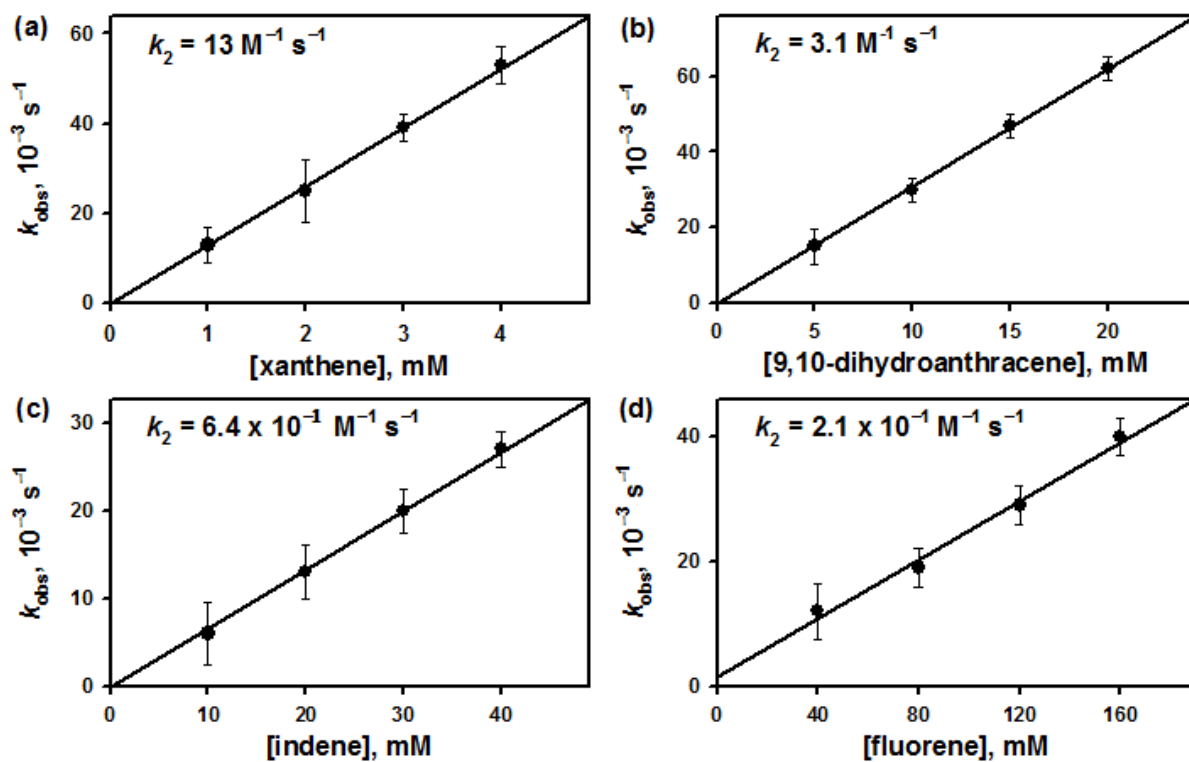


**Figure S15.** Plots of  $k_{\text{obs}}$  against the concentration of substrates [(a) xanthene, (b) 9,10-dihydroanthracene, (c) indene, and (d) fluorene] in order to determine second-order rate constants in the C–H bond activation by **2** in  $\text{CH}_3\text{CN}$  at  $15^\circ\text{C}$  (also see Table S5).

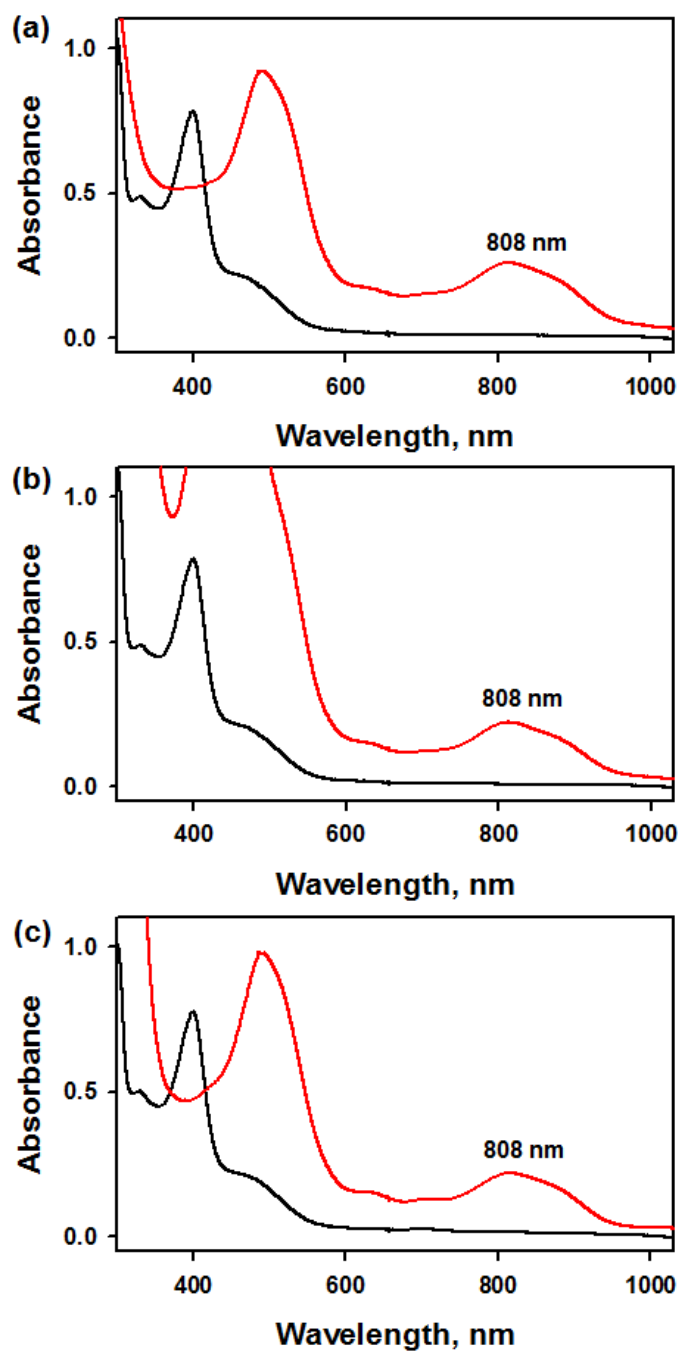


**Figure S16.** UV-vis spectral changes observed in the one-electron oxidation of  $[\text{Fe}^{\text{III}}(\text{TAML})]^-$  (0.10 mM) by (a) cerium(IV) ammonium nitrate (CAN, 1.1 equiv), (b)  $[\text{Ru}^{\text{III}}(\text{bpy})_3]^{3+}$  (1.1 equiv), and (c) TBPA (1.1 equiv) in  $\text{CH}_3\text{CN}$  at  $-40\text{ }^\circ\text{C}$ .



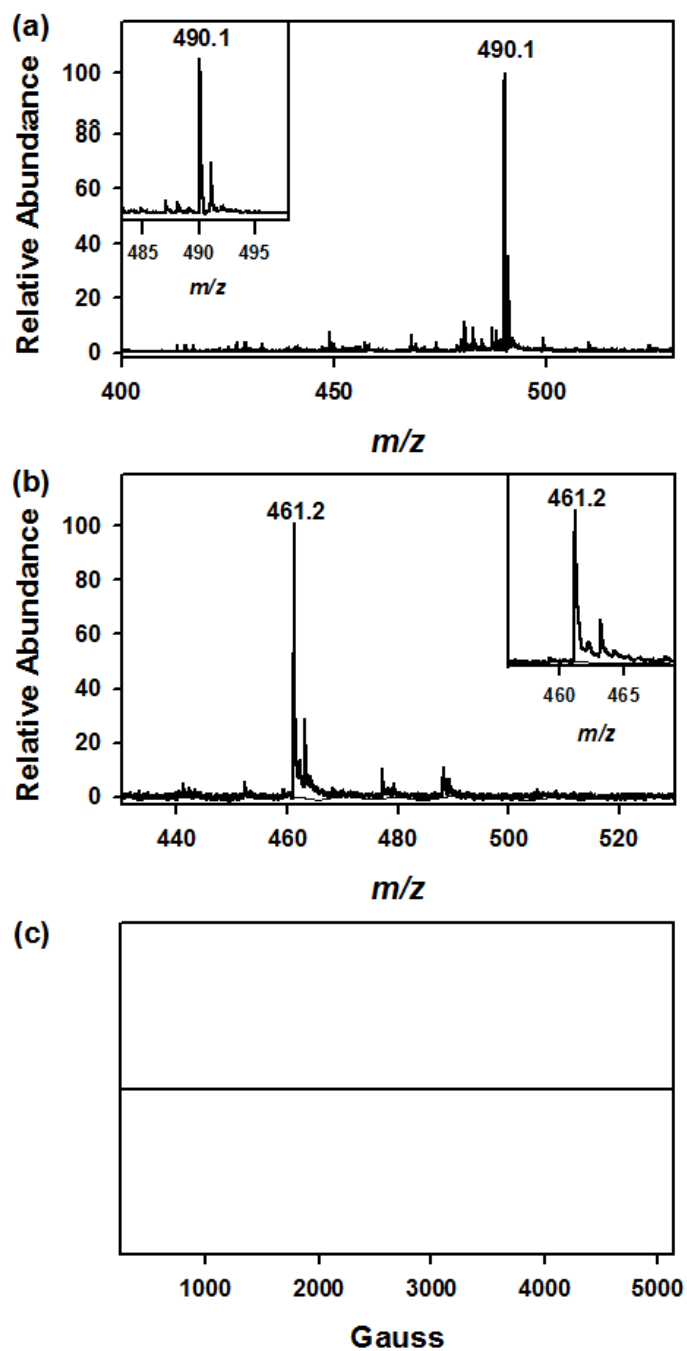


**Figure S17.** CSI-MS spectra [(a) positive and (b) negative modes] of the one-electron oxidized species obtained in the one-electron oxidation of  $[\text{Fe}^{\text{III}}(\text{TAML})]^-$  (0.10 mM) by CAN (0.11 mM), in  $\text{CH}_3\text{CN}$  at  $-40\text{ }^\circ\text{C}$ . The peaks at  $m/z = 490.1$  and  $461.2$  correspond to  $\{\text{Na}[\text{Fe}^{\text{IV}}(\text{TAML})(\text{CH}_3\text{CN})]\}^+$  (calculated  $m/z = 490.1$ ) and  $[\text{Fe}(\text{TAML})(\text{Cl})]^-$  (calculated  $m/z = 461.1$ ), respectively. (c) X-band EPR spectrum of the one-electron oxidized species obtained in the one-electron oxidation of  $[\text{Fe}^{\text{III}}(\text{TAML})]^-$  (0.10 mM) by CAN (1.1 equiv). Spectrum was recorded at 5 K.

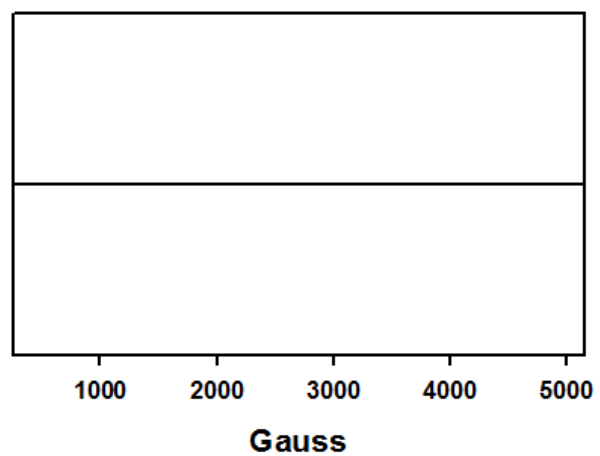


**Figure S18.** X-band EPR spectrum of the complete reaction solution obtained in the oxidation of xanthene (10 mM) by **2** (0.50 mM) in CH<sub>3</sub>CN at 15 °C. Spectrum was recorded at 5 K.

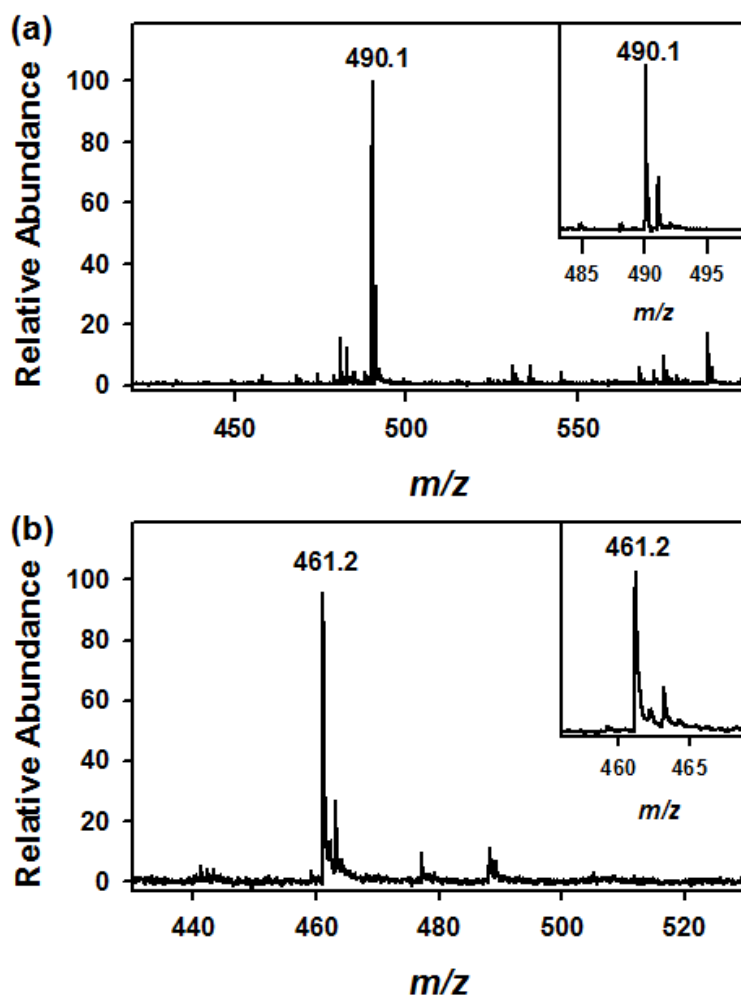


**Figure S19.** CSI-MS spectra [(a) positive and (b) negative modes] of the complete reaction solution obtained in the oxidation of xanthene (10 mM) by **2** in CH<sub>3</sub>CN at -40 °C. The peaks at  $m/z = 490.1$  and  $461.2$  correspond to  $\{\text{Na}[\text{Fe}^{\text{IV}}(\text{TAML})(\text{CH}_3\text{CN})]\}^+$  (calculated  $m/z = 490.1$ ) and  $[\text{Fe}(\text{TAML})(\text{Cl})]^-$  (calculated  $m/z = 461.1$ ), respectively.

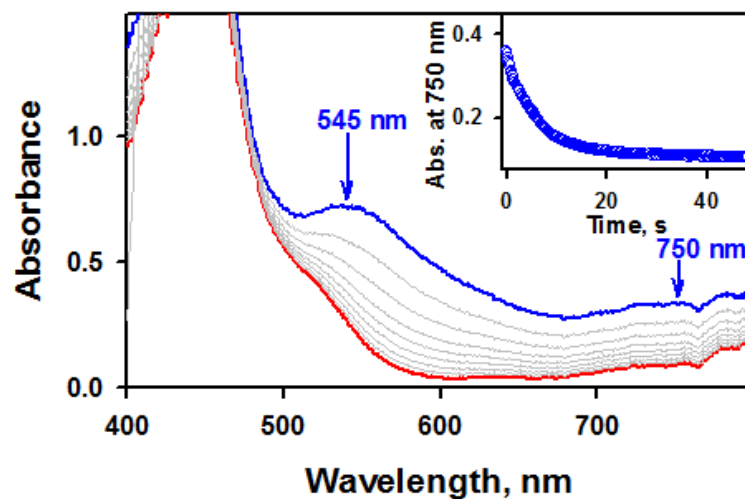


**Figure S20.** UV-vis spectral changes observed in the reaction of **2** (0.10 mM) and thioanisole (5.0 mM) in CH<sub>3</sub>CN at -40 °C. Inset shows the time trace recorded at 750 nm due to **2**.

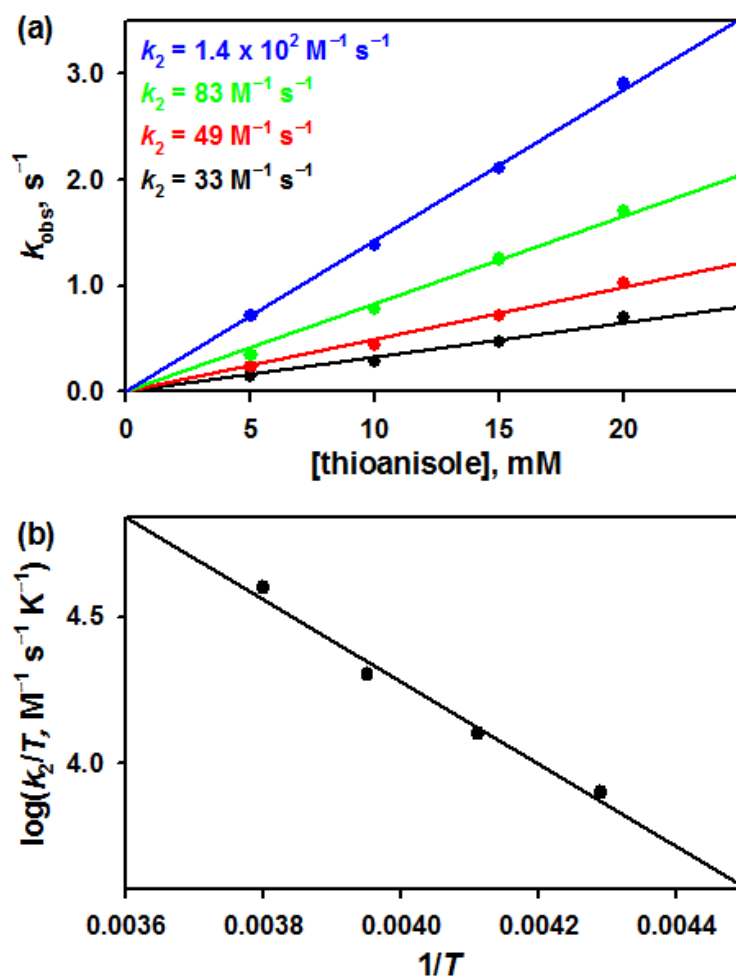


**Figure S21.** (a) Plots of  $k_{\text{obs}}$  against the concentration of thioanisole to determine a second-order rate constant in the sulfimidation reaction by **2** (0.10 mM) in  $\text{CH}_3\text{CN}$  at  $-40$  (black circle),  $-30$  (red circle),  $-20$  (green circle), and  $-10^\circ\text{C}$  (blue circle). (b) Eyring plot of  $\log(k_2/T)$  against  $1/T$  in the reaction of **2** with thioanisole. The  $k_2$  value for **2** at  $15^\circ\text{C}$  was estimated to be  $4.4 \times 10^2 \text{ M}^{-1} \text{ s}^{-1}$  by temperature-dependent kinetics.

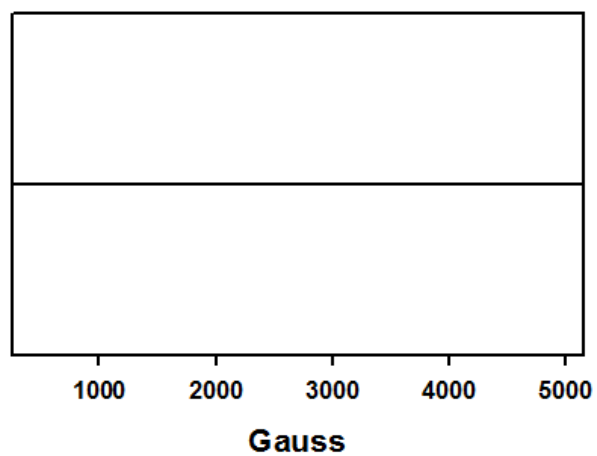


**Figure S22.** X-band EPR spectrum of the complete reaction solution obtained in the oxidation of thioanisole (5.0 mM) by **2** (0.50 mM) in CH<sub>3</sub>CN at -40 °C. Spectrum was recorded at 5 K.

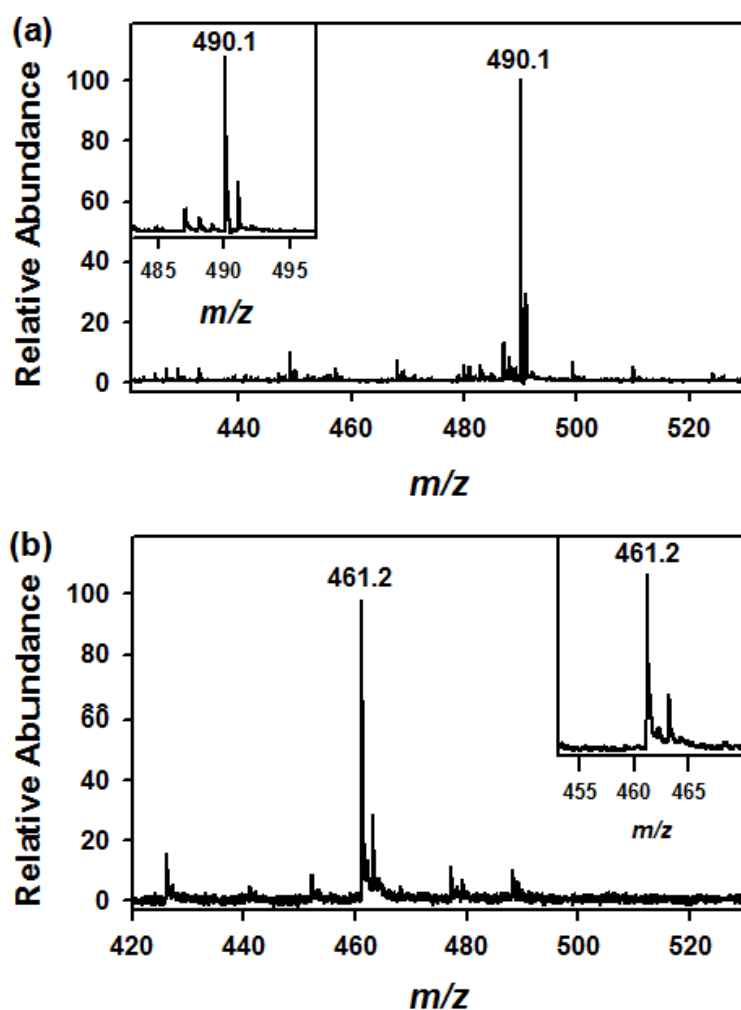


**Figure S23.** CSI-MS spectra [(a) positive and (b) negative modes] of the complete reaction solution obtained in the oxidation of thioanisole (5.0 mM) by **2** in CH<sub>3</sub>CN at -40 °C. The peaks at  $m/z = 490.1$  and  $461.2$  correspond to  $\{\text{Na}[\text{Fe}^{\text{IV}}(\text{TAML})(\text{CH}_3\text{CN})]\}^+$  (calculated  $m/z = 490.1$ ) and  $[\text{Fe}(\text{TAML})(\text{Cl})]^-$  (calculated  $m/z = 461.1$ ), respectively.

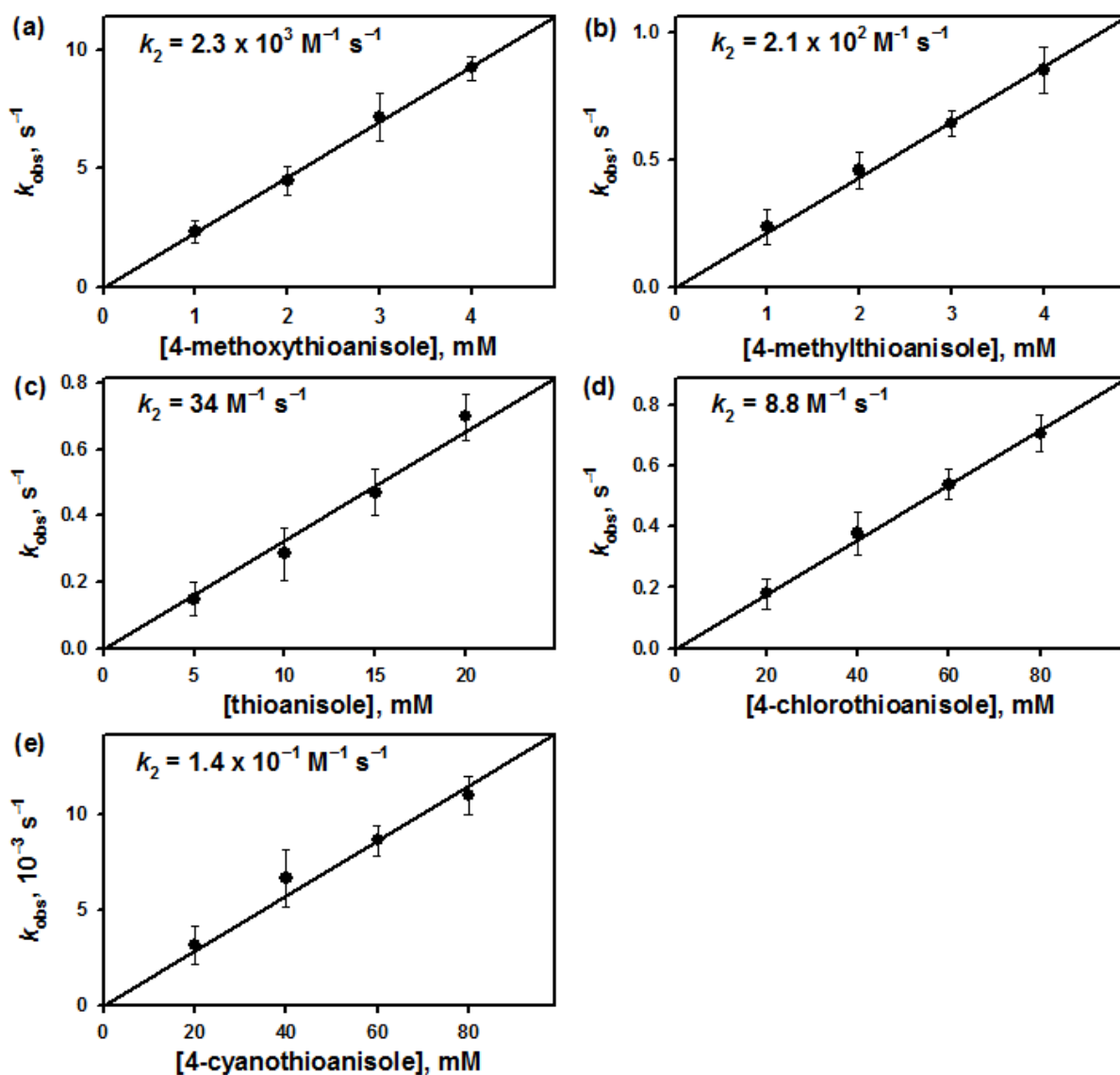


**Figure S24.** Plots of  $k_{\text{obs}}$  against the concentration of substrates [(a) 4-methoxythioanisole, (b) 4-methylthioanisole, (c) thioanisole, (d) 4-chlorothioanisole, and (e) 4-cyanothianisole] in order to determine second-order rate constants in the sulfimidation reactions by **2** in CH<sub>3</sub>CN at -40 °C (also see Table S6).



## References

- S1. Armarego, W. L. F.; Chai, C. L. L. *Purification of Laboratory Chemicals*, 6<sup>th</sup> ed.; Pergamon Press: Oxford, 2009.
- S2. (a) Horwitz, C. P.; Ghosh, A. U.S. Patent 7060818, 2006. (b) de Oliveira, F. T.; Chanda, A.; Banerjee, D.; Shan, X.; Mondal, S.; Que, L., Jr.; Bominaar, E. L.; Münck, E.; Collins, T. J. *Science* **2007**, *315*, 835.
- S3. Taylor, S.; Gullick, J.; McMorn, P.; Bethell, D.; Bulman Page, P. C.; Hancock, F. E.; King, F.; Hutchings, G. J. *J. Chem. Soc., Perkin Trans.* **2001**, *2*, 1714.
- S4. Hong, S.; Sutherlin, K. D.; Vardhaman, A. K.; James, J. J.; Park, S.; Lee, Y.-M.; Jang, S.; Lu, X.; Ohta, T.; Ogura, T.; Solomon, E. I.; Nam, W. *J. Am. Chem. Soc.* **2017**, *139*, 8800.
- S5. Tenderholt, A.; Hedman, B.; Hodgson, K. O. *AIP Conf. Proc.* **2007**, *882*, 105.
- S6. Zabinsky, S. I.; Rehr, J. J.; Ankudinov, A.; Albers, R. C.; Eller, M. J. *Phys. Rev. B* **1995**, *52*, 2995.
- S7. Rehr, J. J.; Mustre de Leon, J.; Zabinsky, S. I.; Albers, R. C. *J. Am. Chem. Soc.* **1991**, *113*, 5135.
- S8. Mustre de Leon, J.; Rehr, J. J.; Zabinsky, S. I.; Albers, R. C. *Phys. Rev. B* **1991**, *44*, 4146.
- S9. Avogadro: an open-source molecular builder and visualization tool. Version 1.XX. <http://avogadro.openmolecules.net/>.
- S10. George, G. N. EXAFSPAK and EDGE-FIT. Stanford Synchrotron Radiation Laboratory, Stanford Linear Accelerator Center, Stanford, CA, **2000**.
- S11. SCM, Vrije Universiteit. *ADF 2014*; SCM: Amsterdam, The Netherlands.
- S12. te Velde, G.; Bickelhaupt, F. M.; Baerends, E. J.; Fonseca Guerra, C.; van Gisbergen, S. J. A.; Snijders, J. G.; Ziegler, T. *J. Comput. Chem.* **2001**, *22*, 931.
- S13. Salomon, O.; Reiher, M.; Hess, B. A. *J. Chem. Phys.* **2002**, *117*, 4729.
- S14. Reiher, M.; Salomon, O.; Hess, B. A. *Theor. Chem. Acc.* **2001**, *107*, 48.
- S15. Becke, A. D. *J. Chem. Phys.* **1993**, *98*, 5648.
- S16. Stephens, P. J.; Devlin, F. J.; Chabalowski, C. F.; Frisch, M. J. *J. Phys. Chem.* **1994**, *98*, 11623.

- S17. Staroverov, V. N.; Scuseria, G. E.; Tao, J.; Perdew, J. P. *J. Chem. Phys.* **2003**, *119*, 12129.
- S18. Tao, J.; Perdew, J. P.; Staroverov, V. N.; Scuseria, G. E. *Phys. Rev. Lett.* **2003**, *91*, 146401.
- S19. Gouré, E.; Avenier, F.; Dubourdeaux, P.; Sénèque, O.; Albrieux, F.; Lebrun, C.; Clémancey, M.; Maldivi, P.; Latour, J.-M. *Angew. Chem., Int. Ed.* **2014**, *53*, 1580.
- S20. Soda, T.; Kitagawa, Y.; Onishi, T.; Takano, Y.; Shigeta, Y.; Nagano, H.; Yoshioka, Y.; Yamaguchi, K. *Chem. Phys. Lett.* **2000**, *319*, 223
- S21. Van Heuvelen, K. M.; Fiedler, A. T.; Shan, X.; De Hont, R. F.; Meier, K. K.; Bominaar, E. L.; Münck, E.; Que, L., Jr. *Proc. Natl. Acad. Sci. USA* **2012**, *109*, 11933.